Article

Berberine-inspired ionizable lipid for self-structure stabilization and brain targeting delivery of nucleic acid therapeutics

Xufei Bian[1,2,3,5], Qian Guo[1,2,5], Lee-Fong Yau [4], Ling Yang[1], Xiaoyou Wang[1], Shikang Zhao[1], Shiqiong Wu[2], Xurong Qin [1], Zhi-Hong Jiang [4] ✉ & Chong Li [1,2] ✉

Lipid nanoparticles have shown success in targeting major organs such as the liver, spleen, and lungs, but crossing the blood-brain barrier (BBB) remains a major challenge. Effective brain-targeted delivery systems are essential for advancing gene therapy for neurological diseases but remain limited by low transport efficiency and poor nucleic acid stability. Here, we report a library of ionizable lipids based on the tetrahydroisoquinoline structure of proto-berberine alkaloids, designed to improve BBB penetration via dopamine D3 receptor-mediated endocytosis. These nanoparticles offer three key advantages: enhanced brain uptake, improved nucleic acid stability through poly(A) self-assembly, and minimal immunogenicity with inherent neuroprotective properties. In murine models, they demonstrate therapeutic potential in Alzheimer's disease, glioma, and cryptococcal meningitis. This berberine-inspired delivery system integrates precise receptor targeting with nucleic acid stabilization, offering a promising platform for brain-targeted therapeutics.

Small-molecule natural products have gained prominence not only as lead compounds in drug development but also as facilitators of drug delivery. Notable examples include the complexation of Herceptin with (−)-epigallocatechin-3-O-gallate (EGCG) for cancer treatment[1], and TANNylation of therapeutic proteins with tannic acid (TA) for targeting elastins and collagens in cardiac therapy[2]. The substitution of cholesterol (Chol) with terpenes, specifically ginsenoside Rg5 in liposomal bilayers, has enhanced GLUT1 receptor targeting in cancer therapy[3]. While various natural compounds including flavonoids, terpenes, coumarins, quinones, and steroids have been explored for drug delivery[4], alkaloids remain underutilized despite their tertiary and quaternary amine structures demonstrating robust interactions with nucleic acid drugs and enhanced biomembrane penetration, as evidenced by their effects on bacterial biofilms[5], cell membranes[6], and organelles[7]. Recently, we reported that lipid nanoparticles (LNPs)

designed with vincamine alkaloids could achieve effective brain targeting by regulating cerebral microvessel blood flow[8]. While this strategy underscores the promise of natural alkaloid-inspired LNP design, certain aspects merit further optimization. For example, reliance on electrostatic interactions alone may not sufficiently address the challenges of efficient nucleic acid drug loading and stability. Furthermore, the ionizable lipid head group in LNPs could be optimized to exhibit stronger affinity for target cells, enabling potent targeting.

Berberine (BE), a prominent isoquinoline alkaloid, and its analogs such as jatrorrhizine, African tetrandrine, and palmatine belong to the family of naturally occurring protoberberine alkaloids[9]. Their reduced derivatives, known as tetrahydroberberine-type alkaloids, obtained through either plant extraction or berberine hydrogenation, exhibit enhanced stability, bioavailability, safety, and therapeutic efficacy[10].

[1]Engineering Research Center of Coptis Development & Utilization, Ministry of Education, College of Pharmaceutical Sciences, Southwest University, Chongqing 400715, PR China. [2]Guangdong-Hong Kong-Macao Joint Laboratory for New Drug Screening, School of Pharmaceutical Sciences, Southern Medical University, Guangzhou 510515, PR China. [3]Medical Imaging Key Laboratory of Sichuan Province, North Sichuan Medical College, Nanchong 637000 Sichuan, PR China. [4]State Key Laboratory of Quality Research in Chinese Medicine, Macau University of Science and Technology, Taipa, Macau 999078, PR China. [5]These authors contributed equally: Xufei Bian, Qian Guo. ✉e-mail: zhjiang@must.edu.mo; chongli@swu.edu.cn

These alkaloids demonstrate both nucleic acid binding capabilities and diverse pharmacological activities, including antimicrobial, anti-inflammatory, antioxidant, and antitumor properties[11]. They show DNA-binding preferences, particularly for thymidine-adenine pairs[12], and interact with mRNA through partial intercalation with poly(A) tails[13] via hydrogen bonding and π-π stacking[14], making them particularly interesting for nucleic acid delivery. Moreover, proto-berberine's specific interactions with cell surface receptors[15,16], notably the dopamine D3 receptor (D3R)[17], offer potential for targeted delivery. D3R is abundant in Alzheimer's disease (AD)-associated regions such as the hippocampus and cortex[18], as well as in the pituitary gland region[19,20], which is prone to brain infections and tumors, making these protoberberine-type alkaloids promising candidates for brain-targeted drug delivery.

Here, we present a series of ionizable lipids inspired by proto-berberine alkaloid architecture, focusing on stable tetra-hydroberberine derivatives (Fig. 1). Our comprehensive validation, from molecular to animal studies, reveals four key advantages of the second-generation alkaloid-based LNP: enhanced nucleic acid loading capacity and stability, improved endosomal escape and intracellular transport of nucleic acid drugs, superior brain-targeting capabilities confirmed both in vitro and in vivo, and retained pharmacological activity from protoberberine alkaloids, enabling synergistic effects with nucleic acid drugs.

Results

Design and screening of BE lipidoids

We designed five tetrahydroisoquinoline alkaloid-inspired head groups (A1-A5) and fifteen tail groups (B1-B15) incorporating diverse structural features, including unsaturated bonds, ester groups, and alcoholic hydroxyl groups for gene delivery (Fig. 2a). The delivery system comprised synthesized ionizable lipids, helper lipids (DSPC, DOPC, or DOPE), Chol, and DMG-PEG$_{2000}$. Twenty-seven BE formulations were prepared with varying molar ratios of ionizable lipids (29–49%), helper lipids (10–30%), Chol (20–59%), and DMG-PEG$_{2000}$ (1–2%), with total molar ratios of 100% for each formulation (Supplementary Table 1).

The screening process involved three phases using blank lipid nanoparticles (LNPs) (Fig. 2b). Initial screening was based on the physicochemical characterizations of BE lipidoids, including particle size and polydispersity index. Using A2-B13 as the representative ionizable lipid, we systematically screened 27 BE formulations with different molar ratios of components. Formulation 10 was identified as optimal, yielding particles with a diameter of 63.94 nm (Supplementary Table 2). Subsequently, BE lipidoids were prepared using 75 combinations of head groups and tail groups based on formulation 10, with 27 combinations showing ideal particle sizes below 100 nm (Supplementary Table 3). These 27 BE lipidoids entered the second screening phase to measure their pKa values, with 10 candidates showing values within the optimal range (6.0–7.0) for effective RNA delivery (Supplementary Fig. 1). In the third phase, we assessed the binding interactions of these 10 BE lipidoids with the poly(A) tail, which is crucial for RNA stabilization[21–23]. Five candidates (A1-B15, A2-B13, A3-B1, A4-B15, and A5-B13) exhibited the highest interaction (Fig. 2c). In vitro targeting experiments demonstrated that the LNPs containing these lipidoids exhibited higher uptake rates than the control group (NP) without ionizable lipids (Fig. 2d, e and Supplementary Table 4). This trend was consistently observed in vivo, with A2-B13 emerging as the most promising BE lipidoid (Fig. 2f, g and Supplementary Figs. 2, 3a). Its structural characterization was
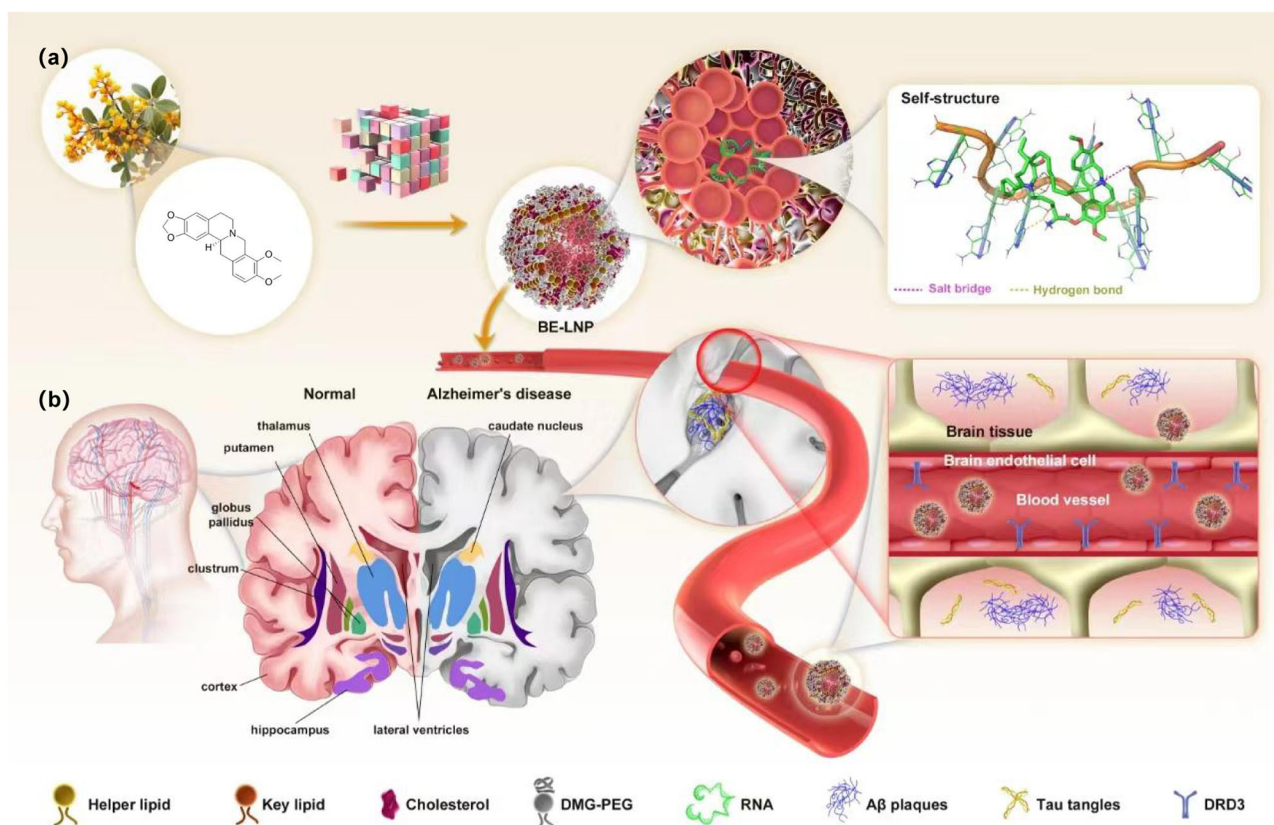

Fig. 1 | **Design and mechanism of berberine-inspired lipidoid nanoparticles (BE) for targeted brain delivery. a** Construction of a three-dimensional combinatorial synthesis library and formation of BE@RNA complexes through berberine derivative-poly(A) affinity and self-assembly properties. **b** Blood-brain barrier penetration mechanism through dopamine D3 receptor (D3R)-mediated transport, enabling targeted therapeutic delivery for neurodegenerative disorders, including Alzheimer's disease.
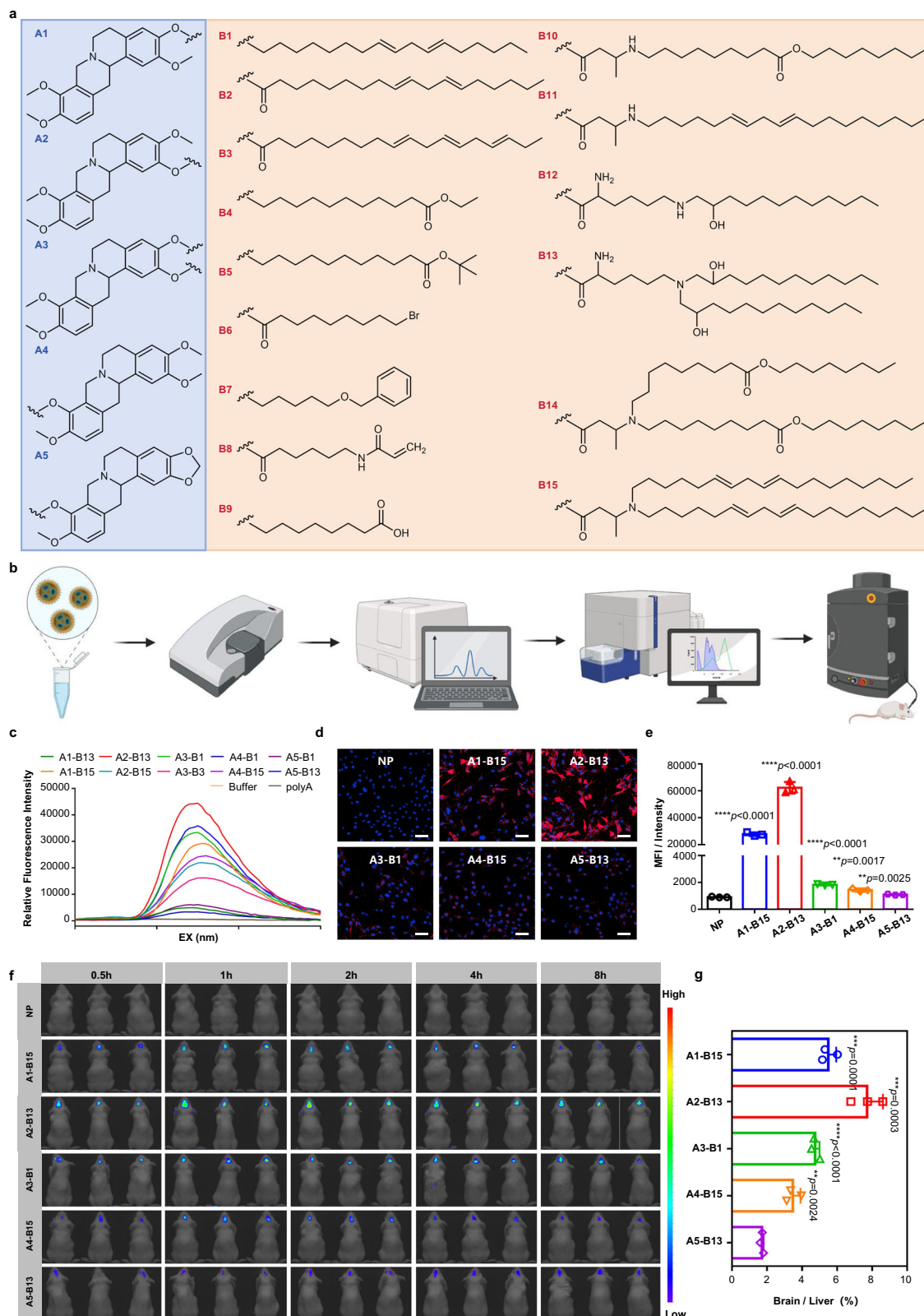
Fig. 2 | Design and characterization of tetrahydroisoquinoline alkaloid-based ionizable lipids. a Chemical structures of lipid building blocks comprising five amine heads and 15 alkylated tails. **b** Optimization workflow for BE lipidoid molecule development, involving 27 formulations derived from 75 novel ionizable compounds. (Created with BioRender.com) **c** Affinities of various ionizable lipidoid molecules for poly(A) measured using fluorescence spectroscopy. **d**, **e** Cellular uptake of LNPs assessed by fluorescence co-localization studies and flow cytometry analysis. LNPs were labeled DiD (red). Nuclei were stained with Hoechst 33342 (blue). Scale bar, 20 μm. **f** In vivo imaging of mice after injection of LNP@DiR at 0.5, 1, 2, 4, and 8 h. **g** Ex vivo fluorescence distribution showing brain-to-liver ratio at 1 h. Data are presented as mean ± SD ($n = 3$ independent experiments). Statistical significance was determined by two-tailed unpaired Student's t test (two groups) or one-way ANOVA with Dunnett's multiple comparison tests (multiple groups); **$P < 0.01$, ***$P < 0.001$, ****$P < 0.0001$. Source data are provided as a Source Data file.
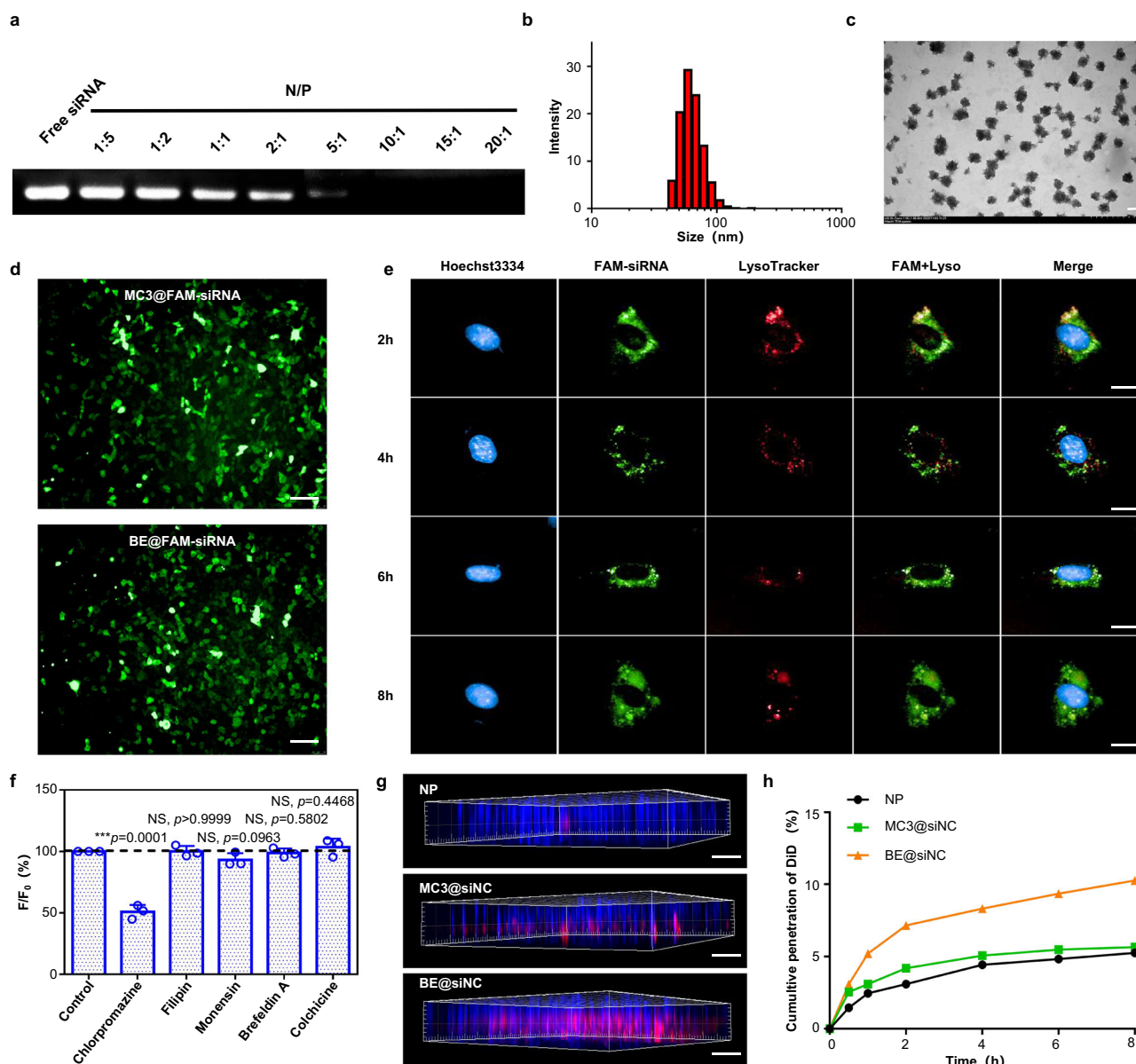
Fig. 3 | In vitro characterization of BE-based LNPs containing ionizable lipid A2-B13. a Gel retardation assay of BE@siRNA at LNP/siRNA weight ratios from 0.2 to 20 to evaluate complex stability. **b** Size distribution analysis by dynamic light scattering. **c** Transmission electron microscopy (TEM) image showing particle morphology of BE@siRNA. Scale bar, 100 nm. **d** Cellular uptake comparison between BE@FAM-siRNA and MC3@FAM-siRNA by fluorescence microscopy. Scale bar, 25 μm. **e** High-magnification imaging of subcellular localization of BE@siRNA and MC3@siRNA. FAM channel shows BE@FAM-siRNAs (green). LysoTracker channel shows lysosome (red). Nuclei were counter stained with Hoechst 33342 (blue). Scale bar, 5 μm. **f** Analysis of BE-mediated endocytosis mechanisms. **g, h** LNP@DiD penetration across an in vitro blood-brain barrier (BBB) model using transwell assays. LNPs were labeled DiD (red). Nuclei were counter stained with Hoechst 33342 (blue). Scale bar, 1000 μm. Data are presented as mean ± SD ($n = 3$ independent experiments). Statistical significance was determined by two-tailed unpaired Student's t test (two groups) or one-way ANOVA with Dunnett's multiple comparison tests (multiple groups); ***$P < 0.001$; NS not significant. Data are representative of three (**c, d**) and two (**e**) independent experiments with similar results. Source data are provided as a Source Data file.

confirmed by ^{1}H nuclear magnetic resonance (NMR) analysis (Supplementary Fig. 4).

Preparation and characterization of BE@siRNA

Following systematic screening, we identified A2-B13 as the lead structure and optimized its formulation composition (molar ratio: A2-B13:DOPC:Chol:DMG-PEG$_{2000}$ = 39:30:30:1). Gel retardation assays demonstrated effective siRNA (siNC, negative control) entrapment by BE at LNP/siRNA ratios above 1:2 (Fig. 3a). DLS analysis and TEM revealed spherical morphologies with hydrodynamic diameters about 70 nm for BE and 90 nm for BE@siRNA complexes (Fig. 3b, c). The transfection efficiency of BE was evaluated using FAM-labeled siRNA,

showing comparable efficacy to the commercial lipidoid DLin-MC3-DMA, as demonstrated by similar intracellular fluorescence intensities (Fig. 3d and Supplementary Fig. 5a). Intracellular trafficking studies using confocal microscopy revealed substantial co-localization with early endosomal markers and reduced presence in late endosomes and lysosomes, indicating efficient endosomal escape (Fig. 3e and Supplementary Fig. 5b, c).

Investigation of the endocytic pathway using specific inhibitors showed that chlorpromazine significantly suppressed BE@DiD uptake, suggesting a primarily clathrin-mediated cellular entry mechanism (Fig. 3f). Using an in vitro transwell model, we demonstrated enhanced blood-brain barrier penetration of BE formulations compared to NP

and MC3 (Fig. 3g, h and Supplementary Fig. 6). The transcytosis mechanism was confirmed to be clathrin-dependent, as evidenced by inhibitor studies using colchicine and chlorpromazine.

Brain targeting of BE+Scutellarin (BE-ST)

Flow cytometry analysis revealed that BE exhibited 65.84-fold enhanced cellular uptake compared to NP (Fig. 2e), substantially exceeding the 0.2- to 1.6-fold improvements typically observed with classical targeting ligands[24–28]. To investigate the mechanism, we knocked down DRD3 protein expression using siRNA, achieving approximately 50% reduction after 72 h (Supplementary Fig. 7). The subsequent decrease in BE uptake in DRD3 knockdown cells (Fig. 4a) indicated receptor-mediated endocytosis. Mechanistic studies revealed that BE functioned as a DRD3 receptor antagonist by decreasing cyclic adenosine monophosphate (cAMP) levels without altering DRD3 expression or stability, consistent with previous findings[17] (Supplementary Figs. 8, 9, 10a–e and Tables 5, 6).

To optimize brain targeting, we developed an acid-base pair strategy using organic acids including scutellarin (ST)[29], EGCG[30], and citric acid (CA)[31] to neutralize the positive charge of BE (Fig. 4b). Among these, ST complexation maintained BE's DRD3 binding affinity and BBB penetration capability (Supplementary Fig. 10f–h and Tables 7, 8), while achieving a brain-to-liver distribution ratio of approximately 20% (Fig. 4c, d and Supplementary Fig. 3b). The BE-ST formulation demonstrated improved pharmacokinetics with higher peak plasma concentration and a 1.73-fold increased half-life compared to BE alone (Fig. 4e).

In vivo evaluation using DiR-labeled LNPs showed superior brain accumulation of BE-ST nanoparticles compared to control formulations (Fig. 4f and Supplementary Fig. 3c, d). Time-course ex vivo imaging and biodistribution studies (1-8 h post-injection) demonstrated that BE-ST achieved stronger brain signals than the clinical-stage brain-targeting formulation glutathione-modified nanoparticles (GSH-NP)[32] (Fig. 4g and Supplementary Figs. 11–13). Quantitative analysis confirmed that BE-ST achieved 167% higher brain accumulation compared to GSH-NP (Fig. 4h and Supplementary Fig. 14).

Brain-targeted delivery of siBACE1 by BE-ST for AD treatment

We evaluated the BE-ST delivery system using AD as a murine models of the disease, targeting beta-site amyloid precursor protein-cleaving enzyme 1 (BACE1)[33]. APP/PS1 mice received bilateral caudal vein injections of BE-ST@siBACE1 (siRNA, 1 mg/kg) or control BE-ST@siScr (scrambled siRNA), with MC3@siBACE1 serving as comparative control (Fig. 5a). PBS-injected APP/PS1 and wild-type (WT) mice were used to establish baseline AD-related deficits.

Morris water maze (MWM) testing revealed that PBS and MC3@siBACE1-treated mice displayed undirected search patterns, indicating no cognitive improvement (Fig. 5b), with comparable swimming speeds across groups (Fig. 5e). Conversely, BE-ST@siBACE1-treated APP/PS1 mice demonstrated marked improvement, spending 1.95 times longer in the target quadrant and crossing it more frequently compared to PBS-treated controls (Fig. 5c, d).

Post-behavioral analysis of brain tissue revealed that BE-ST@siBACE1 treatment significantly reduced hippocampal and cortical BACE1 levels (Fig. 6a, b and Supplementary Fig. 15a). We observed decreased amyloid plaque number and size in hippocampus, cortex, and serum (Fig. 6c and Supplementary Fig. 16). Hyperphosphorylated tau protein (p-tau) levels were also reduced in hippocampus and cortex compared to PBS controls (Fig. 6a, b and Supplementary Fig. 15b).

Protoberberine and its derivatives are known for their synergistic effects on p-tau and Aβ through glycogen synthase kinase-3β (GSK-3β) inhibition[34,35]. This interaction regulates Ser9 phosphorylation and affects BACE1 activity[35]. Our findings revealed significantly reduced phosphorylation at Ser9 of GSK3β (p-GSK3β) in both hippocampus and cortex of APP/PS1 mice treated with BE-ST@siBACE1 and BE-

ST@siScr, compared to the untreated AD group (Fig. 6a, b and Supplementary Fig. 15c). This reduction suggests BE-ST maintains its inhibitory effect on GSK-3β and BACE1, corroborating behavioral improvements in BE-ST@siScr-treated APP/PS1 mice. Gene expression analysis showed significant BACE1, tau, and GSK-3β suppression in hippocampus following BE-ST@siBACE1 treatment (Supplementary Fig. 17a–c). Pearson correlation analysis (Supplementary Fig. 17d–j), combined with cognitive and histopathological improvements, indicated BACE1 silencing as the primary effect rather than modulation of other neurodegeneration-associated pathways.

BE-ST@siScr and BE-ST@siBACE1 treatment reduced superoxide dismutase (SOD), malondialdehyde (MDA), and core proinflammatory cytokine levels in APP/PS1 mice, alleviating oxidative stress (Supplementary Fig. 18a, b) and inflammatory milieu (Supplementary Fig. 18c–f). BE-ST and BACE1 significantly preserved neuronal integrity and morphology, preventing substantial neuronal shrinkage (Fig. 6d). The designed lipid nanoparticles effectively delivered nucleic acids to astrocytes, neurons, and microglia, the desired cell types for AD therapy (Supplementary Figs. 19, 20).

Blood biochemistry and histological analyses two weeks post-injection showed no significant differences between PBS and BE(-ST) @siRNA groups (Supplementary Figs. 21, 22 and Tables 9, 10). Immunogenicity markers including C5b9, C3a, and monocyte chemoattractant protein (MCP-1) remained stable after BE(-ST) treatment (Fig. 6e–g). In contrast, MC3-treated groups showed significant deviation from baseline, consistent with previous reports of LNPs containing DLin-MC3-DMA triggering immune system activation[36]. Real-time quantitative single-cell detection showed that BE induced significantly lower ROS levels compared to commercial MC3 (Supplementary Fig. 23), highlighting BE(-ST)'s favorable safety profile.

BE-ST as a versatile platform for brain disease drug delivery

We investigated BE-ST's versatility across multiple pathological models using different therapeutic agents. In a GL261-Luc brain tumor murine model, we evaluated siVEGF delivery efficacy (Supplementary Fig. 24a). Living imaging showed decreased luminescence following BE-ST@siVEGF treatment. Quantitative analysis revealed significant reductions in mean fluorescence intensity (MFI) of brain tumors with BE-ST treatment: 27.96% at day 3 and 38.82% at day 6 post-administration compared to MC3-treated groups (Supplementary Fig. 24b, c). Ex vivo imaging confirmed BE-ST's enhanced lesion-site targeting (Supplementary Fig. 24d), indicating its potential for siRNA delivery in brain tumor treatment.

We extended our investigation to small-molecule drugs and mRNA across cancer and neurodegenerative disease models. For fungal meningitis, an increasingly prevalent condition with high mortality due to poor BBB penetration of conventional treatments like amphotericin B (AMB), we evaluated AMB-loaded LNPs (NP, GSH, and BE) with comparable encapsulation efficiencies (Supplementary Table 11). We assessed AMB cumulative release (Supplementary Fig. 25) against cryptococcal meningitis (Fig. 7a and Supplementary Fig. 26). The similar drug susceptibility of *C. neoformans* and *C. neoformans*-Luc strains was confirmed by minimum inhibitory concentration determination (Supplementary Table 12). BE-ST@AMB administration enhanced AMB delivery and efficacy, as demonstrated by reduced luminescence. MFI quantification showed brain luminescence decreased by 94.15% at day 3 and 99.28% at day 6 post-treatment compared to AMBisome-treated groups (Fig. 7b, c). Brain fungal burden analysis showed recovery in BE-ST@AMB-treated mice, contrasting with extensive cryptococcal infiltration in untreated or AMBisome-treated mice (Fig. 7d). Long-term studies demonstrated superior survival rates in BE-ST-treated mice (Fig. 7e).

For mRNA applications, BE encapsulating eGFP mRNA showed enhanced transfection efficiency compared to DLin-MC3-DMA, as evidenced by increased intracellular fluorescence (Fig. 7f). This
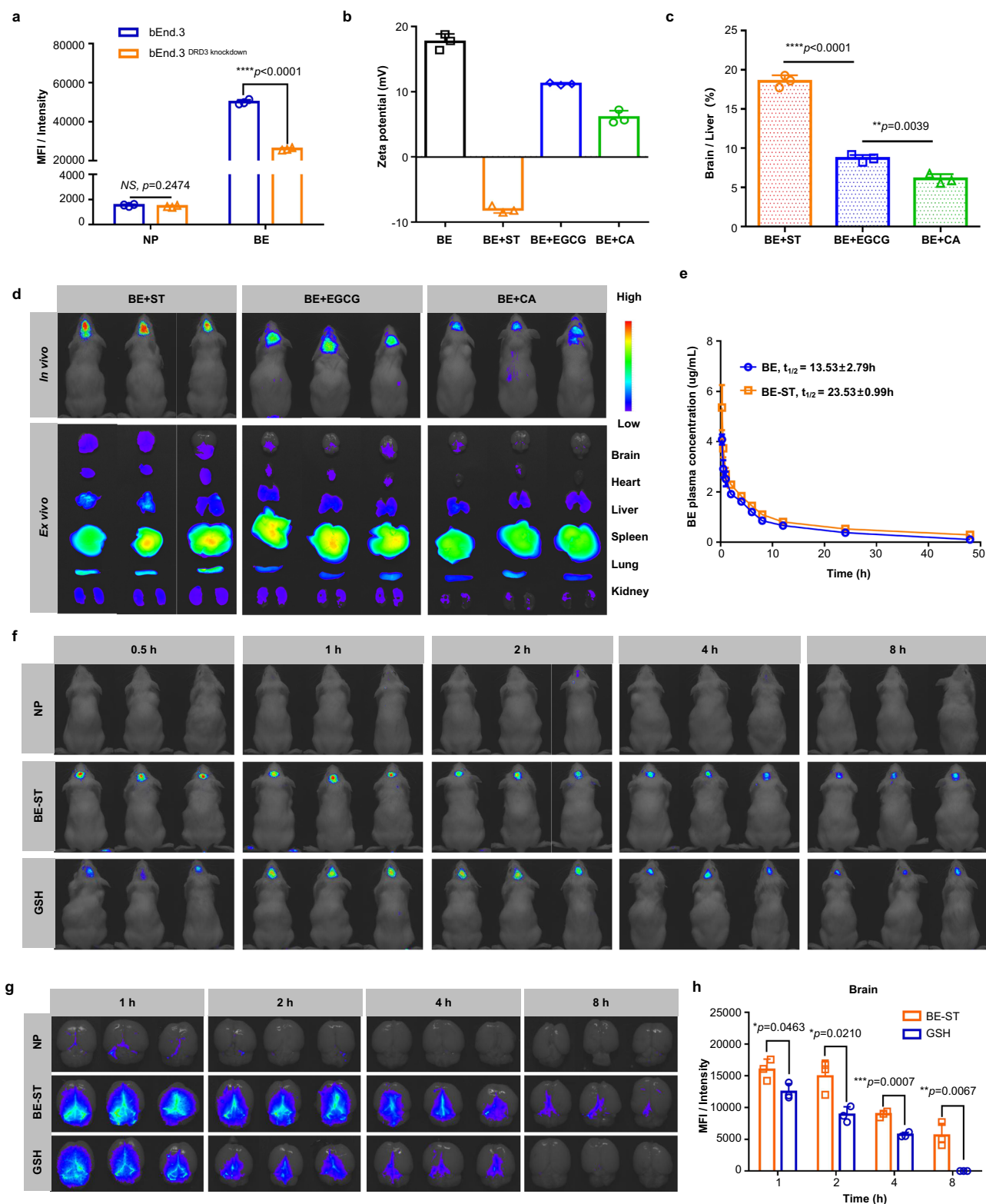
Fig. 4 | Brain-targeting evaluation of BE-ST nanoparticles. a Cellular uptake analysis by flow cytometry following DRD3 knockdown with siRNA. **b** Zeta potential measurements of BE complexed with different organic acids. **c** Brain-to-liver fluorescence distribution ratio of BE formulated with various organic acids by ex vivo imaging. **d** In vivo and ex vivo imaging of LNP@DiR distribution 1 h post-injection of BE-organic acid complexes. **e** Plasma concentration-time profiles of BE and BE-ST (1:5 w/w) in SD rats following intravenous administration. **f** Time-course in vivo imaging of LNP@DiR distribution at 0.5, 1, 2, 4, and 8 h post-injection. **g** Ex vivo brain imaging at 1, 2, 4, and 8 h post-administration. **h** Quantitative analysis of brain fluorescence intensity over time. Data are presented as mean ± SD (*n* = 3 independent experiments). Statistical significance was determined by two-tailed unpaired Student's *t* test; *$P < 0.05$, **$P < 0.01$, ***$P < 0.001$, ****$P < 0.0001$; NS not significant. Source data are provided as a Source Data file.
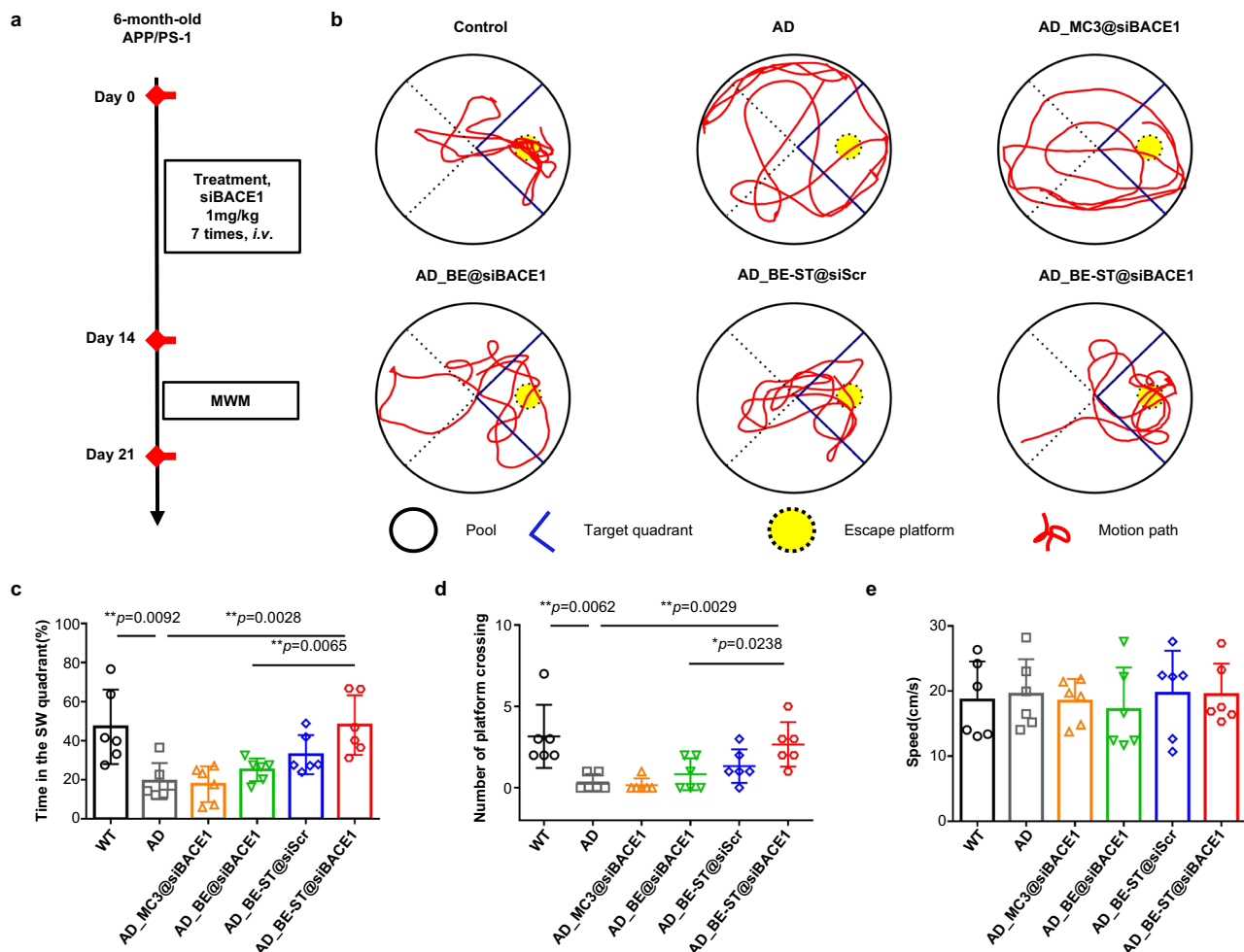
Fig. 5 | BE(-ST)@siBACE1 therapy improves cognitive function in APP/PS1 mice.
a Experimental timeline showing treatment regimen of APP/PS1 and wild-type (WT) mice receiving tail vein injections of LNP@siBACE1 or PBS every 2 days for seven cycles, followed by Morris water maze (MWM) testing and tissue collection. **b−e** MWM probe test results: **b** Representative swimming trajectories during platform search. **c** Time spent in target quadrant as percentage of total time. **d** Platform location crossing frequency. **e** Mean swimming speed across groups. Data are presented as mean ± SD ($n = 6$ biologically independent animals). Statistical significance was determined by two-tailed unpaired Student's t test; *$P < 0.05$, **$P < 0.01$, ***$P < 0.001$. Source data are provided as a Source Data file.

superiority likely stems from strong BE-poly(A) affinity, supported by previous studies[37,38] and molecular docking analyses (Fig. 7g, h and Supplementary Figs. 27, 28, Table 13). The tetrahydroberberine-derived ionizable lipid in BE maintained this affinity while enhancing mRNA structural stability, eliminating the need for chemical modifications. Intravenous BE-ST@eGFP mRNA administration achieved deeper brain penetration and higher fluorescence compared to MC3@eGFP mRNA (Fig. 7i).

Discussion

In the evolving landscape of ionizable lipid designs[39], conventional strategies have favored simple linear tertiary amine groups for enhanced pH sensitivity due to reduced steric hindrance. In fact, nitrogen-containing heterocyclic ring head groups do not necessarily exhibit steric hindrance and may even play a better role in superior binding interactions with nucleic acids. Recently, our work introduced the indoline-fused polycyclic ring structure of the natural alkaloid vinpocetine, demonstrating its ability to enable efficient nucleic acid loading and providing a new structural type for the design of ionizable lipids head groups[8]. Leveraging the nucleic acid complexation capabilities of the protoberberine family[12,37,40–43], we developed an ionizable lipid featuring a dual tetrahydroisoquinoline fused-ring skeleton that binds to RNA poly(A) tails, forming stable self-structures. This approach transcends traditional electrostatic RNA compaction in our recent work[8], enabling efficient nucleic acid loading and endosomal/lysosomal escape while maintaining nucleic acid integrity through partial intercalation without complex chemical modifications.

Synthetic lipidoids often show limited biological performance, with cellular toxicity and immunogenicity[36] being particularly problematic during repeated administration. Tetrahydroisoquinoline derivatives offer inherent pharmacological benefits, including antioxidant and anti-inflammatory properties, potentially mitigating the acute immune response typically associated with RNA therapeutics. These derivatives also function as synergistic therapeutic adjuvants, enhancing overall therapeutic efficacy.

Despite organ-specific targeting advances, the BBB remains challenging. While lipid nanoparticle platforms show promise for targeting the liver[44–47], spleen[46,48], and lungs[49,50], brain targeting presents unique complexities. Traditional strategies employing ligand-receptor interactions via transferrin[51] and peptides including apamin[25], glutathione[32], angiopep-2[52], and RVG peptide[53] typically improve in vitro uptake efficiency by 0.2- to 1.6-fold[24–28] in brain endothelial cells, yet achieve brain-to-liver distribution ratios below 10%.

Our tetrahydroisoquinoline-derived ionizable lipids demonstrate unique BBB penetration capabilities as small molecular ligands. These
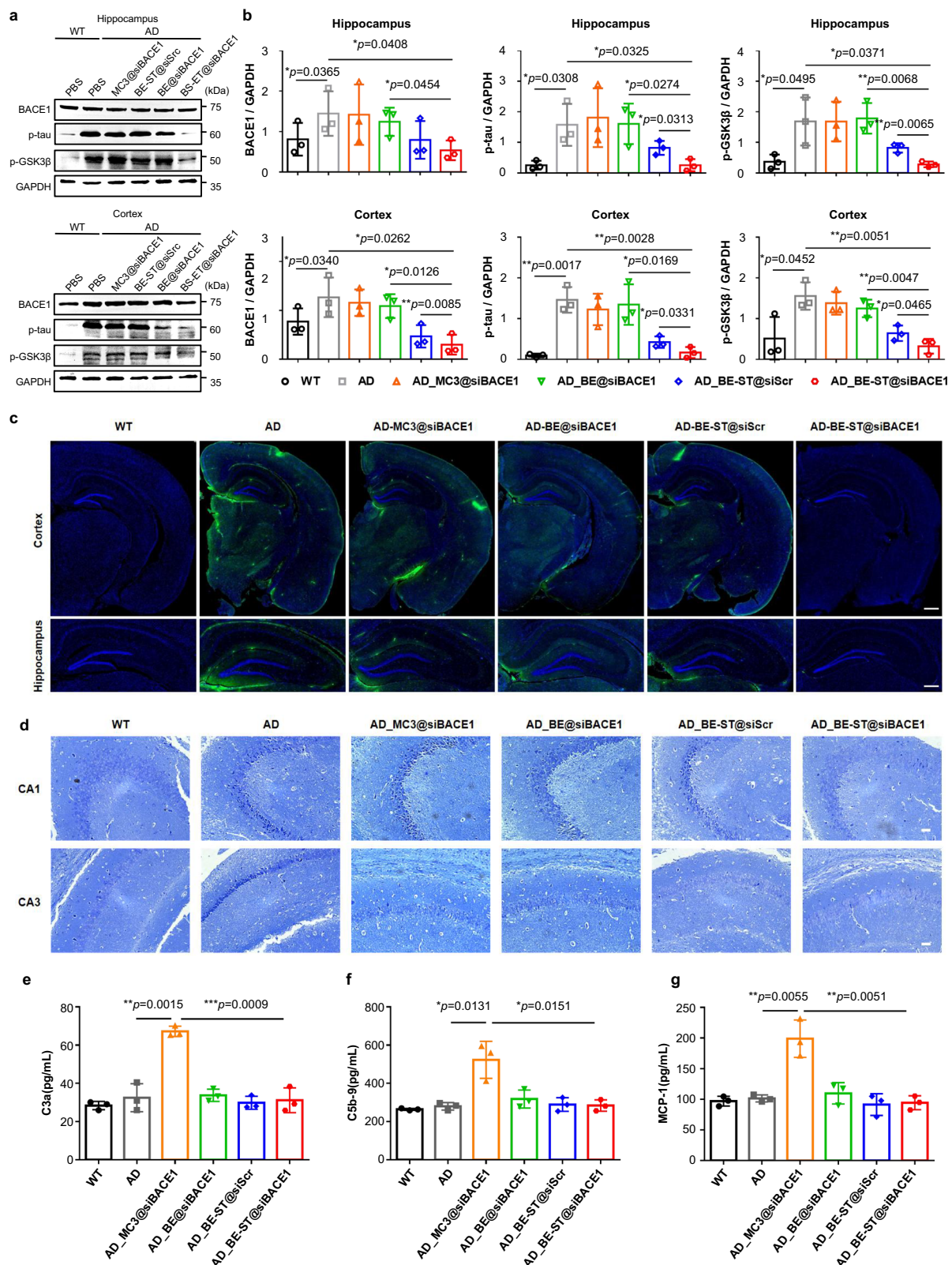
lipids show superior in vitro uptake and exceptional in vivo performance, particularly when combined with organic acids such as ST, EGCG, and CA for charge neutralization. And the design of LNPs in current work still have room for further improvement considering our recently proposed strategy for selectively regulating cerebral blood flow, it might enable both brain 'active distribution' and targeting. In conclusion, the berberine-inspired LNPs effectively deliver siRNA to

the brain and show potential for small molecule and mRNA delivery, suggesting promising applications in neurological therapeutics.

Methods
Statement of ethical regulations
All animal procedures were approved by the Institutional Animal Care and Use Committee (IACUC) of Southwest University Laboratory

Fig. 6 | Therapeutic synergy of BE(-ST) and siBACE1 in modulating Alzheimer's disease (AD) hallmarks in APP/PS1 mice. a Representative western blot images showing BACE1, phosphorylated tau (p-tau), and GSK3β levels in the hippocampus and cortex of BE(-ST)@siBACE1-treated APP/PS1 mice, control APP/PS1 groups, and wild-type (WT) mice. **b** Quantification of western blot for BACE1, p-tau, and phosphorylated GSK3β (p-GSK3β), normalized to GAPDH. The samples derive from the same experiment and that blots were processed in parallel. **c** Representative confocal laser scanning microscopy images showing amyloid-β (Aβ) plaque burden in the hippocampus and cortex of APP/PS1 and WT mice. Aβ

plaques (green) and nuclei (Hoechst 33342, blue). Scale bars: top row, 500 μm; bottom row, 250 μm. **d** Nissl staining of brain sections 14 days post-treatment. Scale bar, 50 μm. ELISA results for complement activation-related pseudoallergy (CARPA) markers: **e** C5b9, **f** C3a, and **g** monocyte chemoattractant protein (MCP-1) in serum. Data are means ± SD ($n = 3$ biologically independent samples). Statistical significance was determined by two-tailed unpaired Student's t test; $*P < 0.05$, $**P < 0.01$, $***P < 0.001$, $****P < 0.0001$. Data in **c**, **d** are representative of two independent experiments with similar results. Source data are provided as a Source Data file.

Animal Center (approval no. IACUC-20230529-02) and conducted in accordance with guidelines established by the Ethical Review Committee of Experimental Animals at Southwest University, China.

Chemicals and reagents

Lipids including DOPC (S01007), DSPC (S01005), DOPE (S03005), DMG-PEG$_{2000}$ (O02005), cholesterol (O01001), and DLin-MC3-DMA (AVT0003) were obtained from AVT Pharmaceutical Tech Co., Ltd. (Shanghai, China). Chlorpromazine hydrochloride (HY-B0407A), filipin complex (HY-N6716), monensin sodium (HY-N0150), brefeldin A (HY-16592), colchicine (HY-16569), and GR 103691 (HY-101382) were purchased from MedChemExpress (Monmouth Junction, NJ, USA). Other chemical reagents were from Energy Chemical (Shanghai, China) or Adamas beta® (Shanghai, China).

siRNA sequences targeting DRD3 (5′-GGUGGAGUCUCGGAAUUU CA-3′), BACE1 (5′-GAACCUAUGCGAUGCGAAUUTT-3′), VEGF (5′-GGA-GUACCCUGAUGAGAUCTT-3′), and control siNC (5′-UUCUCCGAAC-GUGUCACGUTT-3′) were synthesized by Sangon Biotechnology Co., Ltd. (Shanghai, China).

Primary antibodies were obtained as follows: rabbit anti-EEA1 (ab2900, 3 μg ml^{-1}), rabbit anti-LAMP1 (ab208943, 1:100), rabbit anti-Rab5 (ab218624, 1:1000), rabbit anti-GFAP (ab68428, 1 μg ml^{-1}), mouse anti-beta III Tubulin/Tuj1 (ab78078, 1 μg ml^{-1}), rabbit anti-DRD3 (ab155098, 1:5000), rabbit anti-BACE1 (ab183612, 1:1000; ab10716, 1:100) from Abcam (Cambridge, UK); rabbit anti-phospho-GSK3β (Ser9) (PA5-97339, 1:1000) and rabbit anti-phospho-Tau (Ser396) (44-752 G, 1:1000) from Invitrogen (Carlsbad, CA, USA); rabbit anti-Iba1 (019-19741, 1:1000) from Wako (Japan); and rabbit anti-LRP1 (bs-2677R, 1:1000), rabbit anti-TfR (bs-0988R, 1:1000), and rabbit anti-beta amyloid 1-16 (bs-10558R, 1:100) from Bioss Biotechnology Co., Ltd. (Beijing, China); rabbit anti-GAPDH (10494-1-AP, 1:10000) from Proteintech Group, Inc. (Wuhan, China).

Secondary antibodies from Proteintech Group, Inc. (Wuhan, China) included: Cy3-conjugated goat anti-rabbit IgG (SA00009-2, 1:100), Cy3-conjugated goat anti-mouse IgG (SA00009-1, 1:100), multi-rAb CoraLite® Plus 594-goat anti-rabbit IgG (RGAR004, 1:1000), FITC-conjugated goat anti-rabbit IgG (SA00003-2, 1:100), and HRP-conjugated goat anti-rabbit IgG (SA00001-2, 1:5000).

Recombinant mouse D(3) dopamine receptor (Drd3) (CSB-CF007180MO1a2) was from Cusabio (https://www.cusabio.com/, Wuhan, China). Evans Blue (E104208) was obtained from Aladdin Biochemical Technology Co., Ltd. (Shanghai, China). 4% paraformaldehyde (P1110), Hematoxylin-Eosin Stain Kit (G1120), Nissl Stain Kit (G1434) was obtained from Solarbio Science & Technology Co., Ltd (Beijing, China). Lyso-Tracker Red was from KeyGen Biotech (Jiangsu, China). Reactive Oxygen Species Assay Kit (S0033S), Hoechst 33342 (C1022), BeyoECL Star(P0018AS) and BCA Protein Assay Kit (P0012S) was from Beyotime Biotechnology (Shanghai, China). DiD and DiR was from Fluorescence Biotechnology Co. Ltd (Beijing, China). D-Luciferin was from Gold Biotechnology Inc. (St Louis, USA). eGFP mRNA (MR008) was from Novoprotein Scientific Inc. (Shanghai, China).

SteadyPure Universal RNA Extraction Kit II (AG21022), Evo M-MLVRT Mix Kit (AG11728), and SYBR Green Premix Pro Taq HS qPCR Kit (AG11701) were from Accurate Biotechnology Hunan Co., Ltd. (Changsha, China). cAMP ELISA Kit (E-EL-0056) was from Elabscience®

Biotechnology Co., Ltd. (Wuhan, China). Other ELISA kits (ml058756, ml001969, ml037840, EMC001b.96, EMC004.96, EMC101g.96, EMC102a.96) were from Enzyme-linked Biotechnology Co., Ltd. (Shanghai, China) and Neobioscience Technology Co, Ltd. (Shenzhen, China), and biochemical criterion kits (G0904W, G0423W, G0424W, G1202W, G1201W, G1203W, G0101W, G0109W) were from Grace Biotechnology Co., Ltd. (Suzhou, China). All other reagents used were of analytical grade.

Cell culture

bEnd.3 cells (KGG2204-1) were purchased from KeyGen Biotech (Jiangsu, China). GL261-Luc cells (SNLM-547) were obtained from Sunncell Biotechnology Co., Ltd. (Wuhan, China). BV2 (Mouse microglia, CL-0493) and Primary mouse hippocampal neurons[54,55] (CP-M107) were purchased from Procell Life Science & Technology Co. Ltd. (Wuhan, China). Primary brain microvascular endothelial cells (BMEC) and primary astrocytes were obtained from newborn male and female rats (10-day-old). bEnd.3 and GL261-Luc cells were maintained in DMEM medium (KeyGen) supplemented with FBS (Gibco). BV2 cells were cultured in RPMI 1640 medium (KeyGen) supplemented with 20% FBS, 50 U ml^{-1} penicillin, and 50 μg ml^{-1} streptomycin. Primary hippocampal neurons were maintained in Neurobasal-A medium (Procell) containing B-27 supplement and PS. All cells were cultured at 37 °C in a humidified atmosphere with 5% CO_2. bEnd.3$^{DRD3\ knockdown}$ cells were transfected with siDRD3 using Lipofectamine 2000 (Invitrogen).

Cryptococcus neoformans (C. neoformans) strains. The luciferase gene LUC1 was amplified in *C. neoformans* (wild-type H99) from plasmid pCDW104-Luciferase using primers TL1943/1944. The amplified product was cloned into vector pTBL6 to generate pTBL402 (PACTIN-LUC1). The linearized vector (XbaI digestion) was precipitated onto gold microcarrier beads (0.6 μm, Bio-Rad) and introduced into H99 ura5 strain by biolistic transformation[56]. Stable transformants were selected on SD-URA medium.

Animals

The animal experiments were conducted in accordance with the Provision and General Recommendation and approved by the Institutional Animal Care and Use Committee (IACUC) of Southwest University Laboratory Animal Center (approval no. IACUC-20230529-02). Male and female BALB/c mice (5-6 weeks, 18–22 g), C57BL/6 mice (6 months, 28–32 g), and Sprague Dawley (SD) rats (8 weeks, 180–220 g) were obtained from Chongqing Academy of Chinese Materia Medica (Chongqing, China). APP-PS-1 mice (6 months, 28–32 g) were procured from Viewsolid Biotechnology Co., Ltd. (Beijing, China). Animals were kept under pathogen-free conditions at room temperature (22–24 °C) in a humidity-controlled (30–50%) room with a 12 h light/dark cycle. A standard normal chow diet (Jiangsu Xietong Pharmaceutical Bio-engineering Co., LTD, XTI01ZJ-009) and sterile water were given ad libitum. All mice used in experiments throughout the study exhibited normal diet and weight conditions. At the end of the experiment, mice were fully anesthetized with isoflurane and euthanized by decapitation. Mice tissues were immediately removed by dissection.
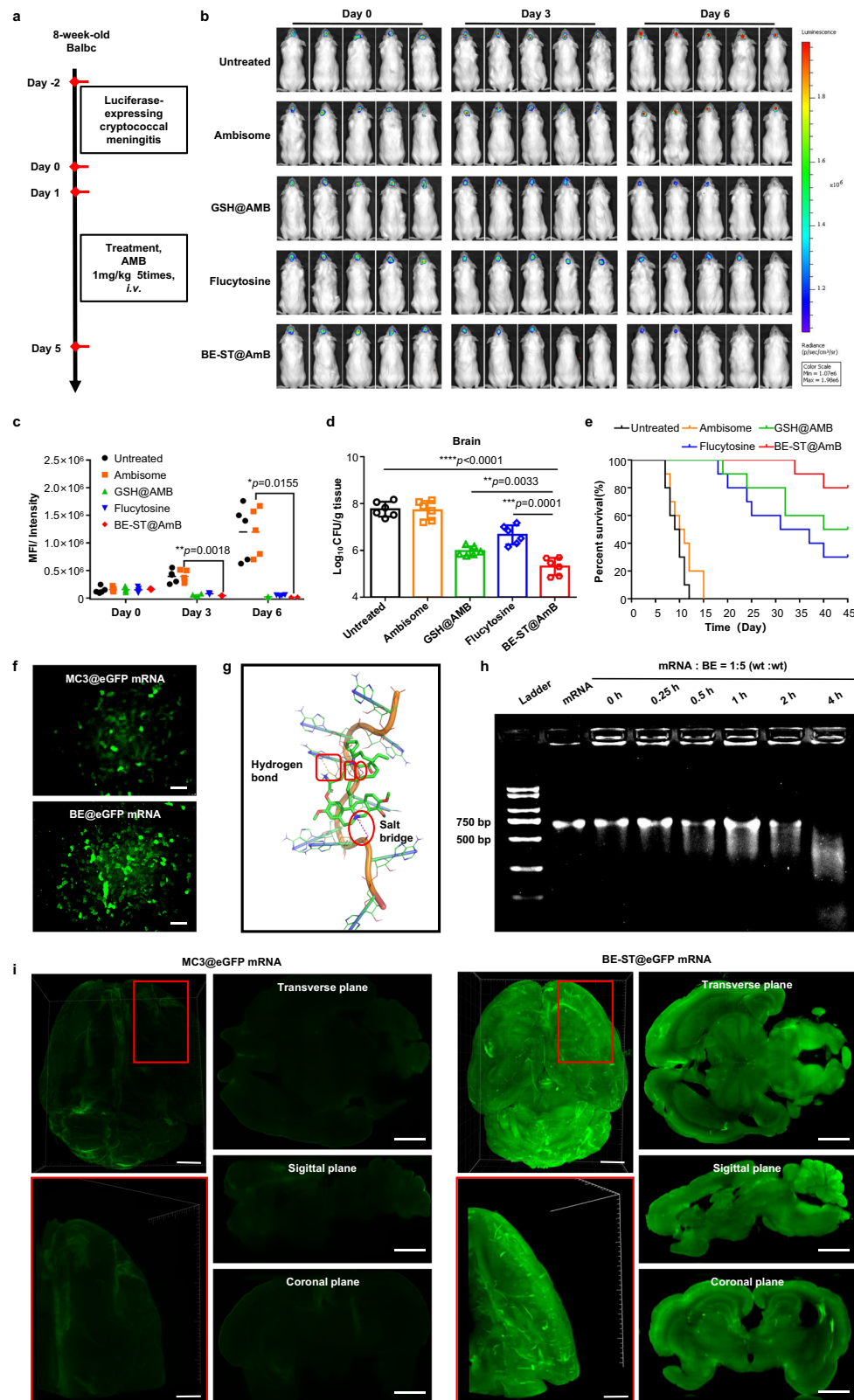
Fig. 7 | BE-ST enables efficient delivery of small-molecule and macromolecular drugs in vivo. a Experimental timeline for cryptococcal meningitis treatment in mice using amphotericin B (AMB). **b, c** In vivo fluorescence imaging and quantification. Data are presented as mean ± SD (*n* = 5 biologically independent animals). **d** Brain tissue fungal colony burden quantification. Data are presented as mean ± SD (*n* = 6 biologically independent animals). **e** Kaplan-Meier survival analysis (*n* = 10 biologically independent animals). **f** Fluorescence microscopy of eGFP mRNA in vitro transfection. Scale bar, 25 μm. **g** Three-dimensional visualization of polyA-A2-B13 binding site interactions (PDB ID: 3GIB). **h** Agarose gel electrophoresis showing BE-loaded mRNA stability. **i** Three-dimensional hyalinization microscopy of brain tissue following 10 μg eGFP mRNA administration. Scale bar, 1500 μm. Statistical significance was determined by two-tailed unpaired Student's *t* test; **P* < 0.05, **P < 0.01, ***P < 0.001, ****P < 0.0001. Data are representative of three (**f**, **h**) and two (**i**) independent experiments with similar results. Source data are provided as a Source Data file.

Synthesis of tetrahydroberberine derivatives

N^6,N^6-bis(2-hydroxy-dodecyl)lysine (180 mg, 0.35 mmol) was dissolved in anhydrous dichloromethane (30 ml). N,N-dicyclohexylcarbodiimide (DCC, 124 mg, 0.6 mmol) and dimethylaminopyridine p-toluenesulfonate (DPTS, 177 mg, 0.6 mmol) were added and stirred under nitrogen (N_2) at room temperature (RT) for 30 min. Tetrahydrotetrandrine (34 mg, 0.1 mmol) in N,N-dimethylformamide (DMF, 2 ml) was then added. The reaction mixture was stirred under N_2 at RT for 24 h and monitored by thin layer chromatography. The product was filtered, concentrated under vacuum, and purified by column chromatography. The structures were confirmed by ^{1}H NMR (400 MHz, Bruker) with the following shifts (DMSO-d_6 + $C_2D_4O_2$): δ 6.98–6.90 (m, 2H), 6.81 (s, 1H), 6.58 (s, 1H), 4.65–4.52 (m, 2H), 4.32–4.22 (d, 1H), 3.81–3.66 (m, 14H), 3.65–3.52 (m, 3H), 2.01–2.81 (m, 8H), 2.81–2.67 (m, 3H), 1.20–1.11 (m, 42H), 0.77–0.73 (m, 6H).

Preparation of BE-LNP

Tetrahydroberberine-derivative lipid nanoparticles (BE-LNP) were prepared using microfluidics. The lipid components, consisting of ionizable lipids selected from our tetrahydroberberine derivatives library and helper lipids including DOPE/DOPC/DSPC optimized for nanoparticle formulation, Chol, and PEG-DMG$_{2000}$, were dissolved in ethanol at ratios specified in Supplementary Table 1. The lipid mixture was combined with siRNA in sodium acetate buffer at 6.25 mM (pH 5.0) at a water-to-ethanol ratio of 3:1 using a microfluidic mixer (AITESEN, China). The resulting mixture was dialyzed overnight against PBS (pH 7.4) to remove ethanol and unincorporated components. The nanoparticles were concentrated using an ultracentrifugal filter (Millipore, Billerica, MA).

Gel retardation assay

siRNA (1 OD) in 125 µl DEPC-treated water was mixed with LNPs at varying weight ratios. After 30 min at RT, complexes containing 500 ng siRNA were mixed with 6× loading buffer and electrophoresed on 2% agarose gel containing 0.02% Goldview stain at 180 V for 20 min in 1× TAE buffer. Gels were analyzed using a gel imaging system (Tanon, China).

mRNA stability assay

mRNA (1 mg ml^{-1}) in DEPC-treated water was mixed with LNPs at a weight ratio of 1:5. Samples were incubated at RT for various times (0, 0.25, 0.5, 1, 2, 4 h). Complexes containing 1.5 µg mRNA were analyzed by gel electrophoresis using 0.02% GelRed stain. Gels were visualized using a gel imaging system.

Physicochemical characterization of BE-LNP

Particle size and zeta potential were measured using dynamic light scattering (DLS) on a Zetasizer (Malvern, England). The morphology of LNPs was examined using transmission electron microscopy (TEM) (Hitachi, Japan).

Acid dissociation constant (pKa) determination

BE-LNP was diluted to 10 mM in PBS. Buffer solution containing 130 mM NaCl, 100 mM ammonium acetate, 10 mM HEPES, and 10 mM MES was prepared and pH-adjusted using 0.1 M NaOH or HCl. In a black 96-well plate (Corning, USA), 95 µl pH-adjusted buffer was mixed with 5 µl BE-LNP and 1 µl TNS solution (100 µM). Fluorescence spectra were recorded at RT using excitation at 321 nm and emission at 445 nm. The pKa was determined as the pH at half-maximum fluorescence intensity.

Poly(A) binding assays

Fluorescence measurements were performed in black 96-well plates at 350 nm excitation. Reactions were conducted in BPES buffer (1.5 mM Na$_2$HPO$_4$, 0.5 mM NaH$_2$PO$_4$, 0.25 mM EDTA, 6 mM NaCl) or citrate-phosphate buffer (5 mM Na$_2$HPO$_4$ adjusted to pH 7.1 and 4.5 with citric acid)[42]. Blank buffer and poly(A)-only controls were included. Fresh solutions of poly(A) (ACTCCCCCAGGTAAAAAAAAAAAAAAAAAAAA AAAAAAAAAAAAAA) and alkaloid were prepared at 10 µM daily.

Cellular uptake and endocytosis mechanism analysis

bEnd.3 and bEnd.3$^{DRD3 knockdown}$ cells were seeded and incubated at 37 °C with 5% CO$_2$ for 12 h. Cells were treated with LNP@DiD formulations for 2 h to assess cellular uptake. For endocytotic pathway analysis, bEnd.3 cells were pretreated with chlorpromazine (12.5 µM), filipin (12.5 µM), monensin (20 µM), brefeldin A (40 µM), colchicine (25 µM), or fresh DMEM for 30 min before adding LNP@DiD and incubating for 2 h at 37 °C. Cells were imaged using a high-content analysis system (Operetta CLS, PerkinElmer, USA). Following trypsinization (0.25%) and PBS washes, cells were resuspended in 300 µl PBS for flow cytometric analysis using flow cytometer (FACSverse, BD) with FlowJo 7.6 software.

Primary astrocyte isolation and culture

Primary astrocytes were isolated from newborn rat cortices following a published protocol[57]. Tissue was dissected under sterile conditions, cleaned, minced, and digested with 0.25% trypsin at RT for 20 min. Non-dissociated tissue was removed by filtration through a sterile nylon mesh. The filtrate was centrifuged at 500 ×g for 10 min and resuspended in complete DMEM containing 10% FBS, then seeded in T25 culture flasks. At 80% confluence, flasks were shaken overnight at 37ºC to remove nonadherent microglial cells, oligodendrocytes, and neurons, followed by gentle washing with complete DMEM. Astrocyte identity was confirmed by GFAP immunofluorescence.

Intracellular transfection and endosomal escape

bEnd.3 cells, astrocytes, neurons, and microglia were seeded and incubated for 12 h at 37 °C with 5% CO$_2$. Cells were treated with LNP@FAM-siRNA formulations in serum-free medium. After incubation, cells were washed thrice with PBS and stained with Hoechst 33342 for 10 min at RT. Astrocytes, neurons and microglia were immunostained with antibodies against GFAP, Tuj1, and Iba1, respectively, followed by Cy3-conjugated goat anti-rabbit IgG. Images were captured using a fluorescence microscope (DMi8, Leica, Germany). bEnd.3 cells were trypsinized (0.25%), washed with PBS, and resuspended in 300 µl PBS for transfection efficiency analysis by flow cytometry.

For subcellular localization, lysosome/endosome was stained by Lyso-Tracker Red for 2 h at 37°C or immunostained with anti-EEA1, anti-Rab5, and anti-LAMP1 at 4 °C overnight followed by fluorescent secondary antibody for 2 h at RT. Cells were then treated with LNP@FAM-siRNA formulations in serum-free medium for 4 h. After incubation, cells were washed thrice with PBS and stained with Hoechst 33342 for 10 min at RT and imaged using confocal microscopy (TCS SP8 DIVE, Leica, Germany).

Molecular docking

Crystal structures of DRD3 (PDB: 3PBL)[58] and poly(A) (PDB: 3GIB)[59] were obtained from RCSB Protein Data Bank. Small molecule three-dimensional structures were constructed and minimized using MMFF94 force field in Chem3D 14.0. Protein structures were prepared with PyMol 2.5.4[60] by removing hydrogen atoms, water molecules, and non-ligand molecules. A binding box was created around the active protein pocket. Molecules were converted to PDBQT format using ADFRsuite 1.0[61]. Docking was performed using AutoDock Vina 1.1.2[62] with conformational search detail of 32. The highest affinity conformation was selected for analysis.

Surface plasmon resonance (SPR) binding assays

DRD3 protein binding kinetics were analyzed using surface plasmon resonance (Nicoya Lifescience, Waterloo, Canada). COOH sensor chips were installed in a system with PBS running buffer at 150 µl min^{-1} flow rate. The system was primed with 80% iso-propyl alcohol to remove

bubbles and stabilize drift signals. DRD3 protein ($25\,\mu g\,ml^{-1}$) was immobilized using standard amine coupling after surface activation with 0.2 M EDC and 0.05 M NHS at $20\,\mu l\,min^{-1}$ for 5 min, followed by ethanolamine blocking. Analytes were injected at $20\,\mu l\,min^{-1}$ with 7 min dissociation monitoring. Chips were regenerated with 10 mM HCl and equilibrated with running buffer for 7 min between injections. GR 103691[63] served as positive control. Affinity constants (K_D) were calculated using Tracedrawer evaluation software by fitting the data to a kinetic model.

Primary brain microvascular endothelial cell (BMEC) isolation and culture

Primary BMECs were isolated from newborn rat following a published protocol[64]. Brain tissue was dissected to remove meninges and choroid plexus, then fragmented and enzymatically digested with collagenase at 37 °C for 30 min under constant shaking. The tissue was mechanically disrupted and filtered through a cell strainer to obtain a single-cell suspension. Cells were centrifuged at 300 ×g for 5 min, resuspended in DMEM/F12 medium supplemented with 10% FBS and 1% PS, and cultured at 37 °C with 5% CO_2. Primary BMECs formed a monolayer within 7-10 days, with medium changes every 2-3 days.

In vitro BBB penetration assay

BMECs were seeded (10,000 cells per well) in the upper chamber of 24-well Transwell plates (Corning, USA). Transendothelial electrical resistance (TEER) was measured using a Millicell-ERS system (Millipore, USA) every two days, with values $>150\,\Omega\,cm^2$ indicating suitable barrier integrity.

After barrier establishment, LNP@DiD formulations were added to the upper chambers and incubated for 0.5-8 h. To investigate transcytosis mechanism, BMECs were pretreated with chlorpromazine (12.5 μM), colchicine (25 μM), or fresh DMEM for 30 min before 8 h incubation with LNP@DiD at 37 °C. Nuclei were stained with Hoechst 33342, and Transwell membranes were mounted on glass slides for imaging using a high-content analysis system and Imaris software. LNP penetration was quantified by measuring basolateral chamber fluorescence using a Multimode Microplate Reader (BioTek Synergy H1, Agilent, USA) at 485 nm excitation and 535 nm emission wavelengths.

To evaluate non-covalent interactions between ST and BE on BBB penetration efficiency, BMECs were treated with BE, ST, BE-ST for 8 h. Samples (50 μl) from upper and lower chambers were mixed with 150 μl methanol, ultrasonicated for 10 min, and centrifuged at 11,000 ×g for 10 min at 4 °C. Supernatant (20 μl) was analyzed by high-performance liquid chromatography (HPLC, SHIMADZU, Japan).

Pharmacokinetic studies

SD rats received BE and BE-ST ($5\,mg\,kg^{-1}$) via tail vein injection. Blood samples (~200 μl) were collected from the orbit at 0.25, 0.5, 1, 2, 4, 8, 12, 24, and 48 h post-injection. Samples were centrifuged at 11,000 ×g for 10 min at 4 °C. Serum (50 μl) was mixed with 150 μl methanol, ultrasonicated for 10 min, and centrifuged under identical conditions. Supernatant (20 μl) was analyzed using HPLC. Pharmacokinetic parameters were calculated using PKsolver 2.0.10 software[65].

In vivo imaging

Brain targeting was evaluated in healthy mice following tail vein injection of LNP@DiR. Fluorescence images were captured at 0.5, 1, 2, 4, and 8 h using the VISQUE in vivo Smart-LF System (Vieworks, Korea) or Lumina III Imaging System (PerkinElmer, USA). Mice were euthanized at predetermined intervals, and major organs were harvested for ex vivo imaging.

For brain tumor model establishment, GL261-Luc cells (5 μl, 10,000 cells μl^{-1}) were stereotactically injected into the right hemisphere over 3 min. After a 10-day post-operation period, mice received daily intravenous injections of LNP@siVEGF ($1\,mg\,kg^{-1}$) for five

consecutive days. Imaging was performed using the Lumina III Imaging System on days 0, 3, and 6 post-injection. For precision targeting analysis, mice received LNP@DiR intravenously and brains were harvested at 8 h post-injection for ex vivo imaging using the VISQUE in vivo Smart-LF System.

For meningitis model development, luciferase-expressing *C. neoformans* (2500 CFU) was injected into mouse brain following the tumor model protocol. After 48 h, mice received daily intravenous injections of LNP@AMB (containing either AMB at $1\,mg\,kg^{-1}$ or flucytosine at $25\,mg\,kg^{-1}$) for five days. Imaging was conducted using the Lumina III Imaging System on days 0, 3, and 6 post-surgery.

Tissue distribution

Healthy mice received intravenous LNP@DiD (100 μg DiD kg^{-1}) via tail vein injection. At 1, 2, 4, and 8 h post-injection, mice were humanely euthanized, and heart, lung, liver, spleen, kidney, and brain tissues were harvested. Weighed tissues were homogenized with methanol (1:3 mass ratio) and centrifuged at 10,000 ×g for 30 min at 4 °C. DiD in the sediment was extracted twice with methanol. The supernatant was analyzed using a Multimode Microplate Reader at 540 nm excitation and 663 nm emission wavelengths.

Evans blue dye exclusion tests

BBB integrity in the fungal brain infection model was assessed using Evans blue dye extravasation. On days 1, 3, 5, and 7, Evans blue dye (2% in saline, 2 ml kg^{-1}) was administered via tail vein injection. After 2 h, deeply anesthetized mice underwent cardiac perfusion with saline (20 ml) followed by 4% paraformaldehyde (20 ml). Isolated brain tissue was photographed, weighed, and homogenized in PBS (1 ml). The homogenate was centrifuged at 10,000 ×g for 10 min at 4 °C. Supernatant (300 μL) was mixed with acetone (700 μL), incubated at RT for 24 h, and centrifuged at 10,000 ×g for 10 min at 4 °C. Absorbance was measured using a Multimode Microplate Reader at 620 nm.

Morris water maze (MWM)

Spatial learning and memory were assessed using the MWM paradigm following established methodologies[66]. The maze comprised a water pool divided into four quadrants, each marked with unique spatial cues (pentagram, square, triangle, or circle) on the quadrant walls. Water temperature was maintained at $22\pm1\,°C$, with food-grade titanium dioxide added for opacity and movement tracking.

Trials were conducted in the afternoon under controlled environmental conditions. Mice were acclimatized to the testing room for 2 h before experiments. The five-day training phase consisted of four daily trials per mouse with 20-30 min inter-trial intervals. Mice were placed facing the pool wall to locate a hidden platform. Platform finding time was recorded, with a 60 s cutoff time. Mice unable to locate the platform were guided to it and allowed 10 s of rest.

A 60 s probe test was conducted 24 h post-training, with the platform removed. Mice were placed facing the quadrant opposite to the target quadrant. EthO Vision XT8.5 tracking software recorded performance metrics, including target quadrant time and platform location crossings, to assess spatial memory retention.

Western blot

For targeted molecular mechanism assessment, bEnd.3 and bEnd.3$^{DRD3\ knockdown}$ cells were collected. Following behavioral assessments, mice were humanely euthanized and perfused transcardially with saline before harvesting the hippocampus and cortex. Samples were homogenized in lysis buffer containing 1% phosphatase inhibitors and 1% PMSF and centrifuged at 12,000 ×g for 15 min at 4 °C. Protein concentration was determined using a BCA Protein Assay Kit.

Protein samples (20 μg) were separated by 10% SDS-PAGE and transferred to PVDF membranes. Membranes were blocked with 5%

nonfat dry milk in Tris-buffered saline at 37 °C for 1 h, then incubated overnight at 4 °C with primary antibodies (BACE1, p-tau, p-GSK3β, DRD3, TfR, LRP1, or GAPDH), followed by HRP-conjugated IgG rabbit secondary antibodies for 1 h at 37 °C. Blots were visualized using ECL, with GAPDH as loading control. Quantification was performed using ImageJ, and results were recorded using a gel image analysis system. Unprocessed scans of the most important blots were provided in the Source Data file.

Real-time PCR

Endogenous BACE1 gene silencing activity of LNP@siBACE1 was investigated by quantitative real-time PCR (qRT-PCR). After 2-week treatments, mice were anesthetized and perfused transcardially with saline. Samples were flash-frozen in liquid nitrogen and stored at -80 °C[67]. Total RNA extraction, reverse transcription, and qRT-PCR were performed according to kit protocols using the ROCGENE Archimed RT-PCR System (Beijing, China). The following primer sequences were used: BACE1 (forward 5'-TACTACTGCCCGTGTCCACC-3', reverse 5'-ACAACCTGAGGGGAAAGTCC-3'), Tau (forward 5'-GAAC-CACCAAAATCCG GAGA-3', reverse 5'-CTCTTACTAGCTGATGGTGAC-3'), GSK3β (forward 5'-TTGGAGCCACTGATTACACG-3', reverse 5'-CCAACTGATCCACACCACTG- 3'), and GAPDH (forward 5'-TTGATGG-CAACAATCTCCA-3', reverse 5'-CGTCCCGTAGACAAAATGGT-3'). GAPDH served as reference housekeeping gene. Relative mRNA expression levels were calculated using the comparative Ct method.

Enzyme-linked immunosorbent assay (ELISA)

Serum analyses were performed on APP/PS-1 transgenic mice following administration every two days for two weeks. Blood samples were collected from the retro-orbital plexus and centrifuged at 2,000 ×g for 10 min at 4 °C to isolate plasma. Samples were stored at -80 °C[68]. To assess potential immune response and toxicity of LNP formulations, amyloid plaque and complement activation-related pseudoallergy (CARPA) indicators (complement C5b-9, C3a, MCP-1) were measured using ELISA kits. Additionally, inflammatory cytokine levels (IL-1β, IL-6, IFNγ, and TNFα) were evaluated using specific ELISA kits to understand the synergistic impact of LNP@siBACE1 on AD.

Blood biochemical profiling

To investigate potential hepatotoxic and nephrotoxic effects of LNP formulations, serum biochemical examinations were performed every other day for two weeks. Blood samples were collected from the retro-orbital plexus and centrifuged at 2000 ×g for 10 min at 4 °C. Plasma was analyzed for biochemical parameters including alkaline phosphatase (ALP), alanine aminotransferase (ALT), aspartate amino-transferase (AST), uric acid (UA), urea (UREA), and creatinine (CREA) to evaluate hepatic and renal function.

Histological staining

APP/PS-1 mice were humanely euthanized following treatment and perfused transcardially. Brains were fixed in 4% paraformaldehyde for 24 h, dehydrated, embedded in OCT, and frozen. Sections (20 µm) were obtained using a high-precision freezing microtome (Leica, Germany). For immunofluorescence, sections were fixed with 4% paraformaldehyde for 30 min, PBS-rinsed, permeabilized with 0.1% Triton X-100 for 15 min, and blocked with 5% BSA for 2 h. Sections were incubated with primary anti-β-amyloid or anti-BACE1 antibody overnight at 4 °C. After three PBS washes, sections were incubated with FITC or 594-conjugated goat anti-rabbit IgG for 2 h at room temperature. For neural cell visualization, sections were stained with antibodies against Tuj1 (neurons), Iba1 (microglia), and GFAP (astrocytes)[69], followed by Cy3-conjugated goat anti-rabbit IgG secondary antibody. Nuclei were counterstained with Hoechst 33342 for 10 min. High-resolution fluorescence images were acquired using confocal microscopy (OLYMPUS FV3000, Japan). Nissl staining was performed to assess neuronal damage. Additionally, vital organs (heart, lung, liver, spleen, and kidney) were fixed in 4% paraformaldehyde, sectioned, and stained with hematoxylin and eosin (H&E). Images were captured using a fluorescence microscope.

Analysis of reactive oxygen species (ROS) levels in single cells

To assess oxidative stress and intracellular ROS levels, a ROS assay kit was utilized. bEnd.3 cells from each treatment group were incubated at 37 °C for 30 min in serum-free medium containing 10 µM DCFH-DA. After incubation, the medium was replaced with fresh medium containing ionizable molecules (5 mg ml⁻¹), and cells were incubated for 2, 12, or 24 h. Cells were then washed three times in PBS containing 0.1% BSA and mounted on glass slides with PBS for microscopy. ROS levels were quantified by measuring cellular fluorescence intensity using a real-time single-cell multimode analyzer with optical fiber probes (Rayme, China).

In vitro release of AMB

In vitro release of AMB from AMB-loaded LNPs (NP, GSH, BE) was evaluated using the dialysis bag method. LNP samples (1 ml) were transferred into dialysis bags (molecular weight cutoff 8,000-14,000 Da) and immersed in PBS containing 0.1% sodium deoxycholate under continuous stirring at 37 °C. Release medium was collected and replaced with fresh medium at predetermined time points (0.5, 1, 2, 4, 8, 12, 24, 48, and 72 h). Samples were centrifuged at 11,000 ×g for 10 min and analyzed by HPLC.

Minimum inhibitory concentration assay

C. neoformans and C. neoformans-Luc were cultured and diluted to 1 × 10⁴ CFU ml⁻¹ in YPD and 1640 medium, respectively. Fungal suspensions (100 µl per well) were transferred to 96-well plates, and drug solution (100 µl) at concentrations ranging from 0-1,024 µg ml⁻¹ were added to corresponding wells. Plates were incubated for 48 h at 30 °C, and OD value was measured at 490 nm using a Multimode Microplate Reader. The minimum inhibitory concentration (MIC) was defined as the lowest concentration inhibiting >90% growth compared with controls.

Tissue burden assessment

Mice were anesthetized and positioned using a stereotactic apparatus for inoculation with 2500 CFU of C. neoformans into the right hemisphere over 3 min, followed by gradual withdrawal. After 48 h, mice received intravenous LNP@AMB. Treatment included daily doses of AMB (1 mg kg⁻¹) or flucytosine (25 mg kg⁻¹) for five consecutive days. On day 6 post-inoculation, mice were euthanized and brains harvested. Brain tissues were weighed and homogenized in sterile saline (1:3 w/v ratio). Homogenates were serially diluted in sterile saline, and 30 µl of each dilution was plated on YPD agar. After 48 h incubation at 30 °C, CFU per gram of brain tissue were determined.

Survival rates study

Mice were inoculated with C. neoformans and after 48 h divided randomly into five groups. Each group received daily intravenous treatments for five days with either saline or LNP@AMB formulations (AMB 1 mg kg⁻¹ or flucytosine 25 mg kg⁻¹). Survival was monitored for 45 days post-treatment.

eGFP-mRNA transfection in vitro

Cells were seeded in 12-well plates and grown to 60 to 70% confluence. Transfection was performed using eGFP mRNA complexed with LNP formulations in serum-free DMEM. After 4 h incubation at 37 °C, medium was supplemented with FBS and cells were incubated for an additional 20 h. eGFP expression was analyzed using fluorescence microscopy.

eGFP-mRNA transfection in vivo

Mice received intravenous LNP@eGFP mRNA (1 mg kg⁻¹). After 24 h, mice were euthanized and brain tissues were fixed in 4% paraformaldehyde for 24 h. Tissue clearing followed established protocols[70]. Tissues were decolorized in 25% v/v Quadrol and 5% v/v ammonium in water at 37 °C for 48 h, followed by delipidation using tert-butanol (tB) solutions (30%, 50%, 70% v/v, pH >9.5 with 3% w/v Quadrol). Tissues were dehydrated in 70% v/v tB, 27% v/v PEG methacrylate Mn500 (PEGMMA500), and 3% w/v Quadrol for 48 h. Final clearing used BB-PEG medium (75% v/v benzyl benzoate, 25% v/v PEGMMA500, 3% w/v Quadrol, refractive index 1.543) until optical transparency was achieved (5-7 days). Cleared samples were preserved at RT in clearing medium and imaged using a light sheet microscope (LiToneXL, Light Innovation Technology, China) equipped with a 43× objective lens (NA = 0.28, working distance = 20 mm). Four-sided illumination was used to capture and merge images for visualization of eGFP expression and distribution.

Statistical analysis

Data are presented as mean ± SD. Statistical significance was determined using unpaired Student's t-tests (two groups) or one-way ANOVA with Dunnett's multiple comparison tests (multiple groups) using GraphPad Prism software (version 8). Statistical significance was set at $p < 0.05$ with 95% confidence intervals. In all figures, where $p < 0.0001$ is indicated, the p-value was too low for Prism software to provide an exact value. Association between BACE1 and p-tau, p-GSK3β gene and protein expression in brain tissues was calculated using Pearson correlation test.

Reporting summary

Further information on research design is available in the Nature Portfolio Reporting Summary linked to this article.

Data availability

The data supporting the findings of this study are available within the paper and its Supplementary Information. Source data are provided with this paper.

References

1. Chung, J. E. et al. Self-assembled micellar nanocomplexes comprising green tea catechin derivatives and protein drugs for cancer therapy. *Nat. Nanotechnol.* **9**, 907–912 (2014).
2. Shin, M. et al. Targeting protein and peptide therapeutics to the heart via tannic acid modification. *Nat. Biomed. Eng.* **2**, 304–317 (2018).
3. Wang, X. et al. Identification and construction of a novel biomimetic delivery system of paclitaxel and its targeting therapy for cancer. *Signal Transduct. Target Ther.* **6**, 33 (2021).
4. Fu, S. & Yang, X. Recent advances in natural small molecules as drug delivery systems. *J. Mater. Chem. B* **11**, 4584–4599 (2023).
5. Yan, Y. et al. Research progress on antibacterial activities and mechanisms of natural alkaloids: a review. *Antibiotics* **10**, 318 (2021).
6. Lebecque, S. et al. Interaction between the barley allelochemical compounds gramine and hordenine and artificial lipid bilayers mimicking the plant plasma membrane. *Sci. Rep.* **8**, 9784 (2018).
7. Patalas-Krawczyk, P. et al. Effects of plant alkaloids on mitochondrial bioenergetic parameters. *Food Chem. Toxicol.* **154**, 112316 (2021).
8. Bian, X. et al. Regulation of cerebral blood flow boosts precise brain targeting of vinpocetine-derived ionizable-lipidoid nanoparticles. *Nat. Commun.* **15**, 3987 (2024).
9. Singh, S., Pathak, N., Fatima, E. & Negi, A. S. Plant isoquinoline alkaloids: advances in the chemistry and biology of berberine. *Eur. J. Med. Chem.* **226**, 113839 (2021).
10. Kim, A. N., Ngamnithiporn, A., Du, E. & Stoltz, B. M. Recent advances in the total synthesis of the tetrahydroisoquinoline alkaloids (2002-2020). *Chem. Rev.* **123**, 9447–9496 (2023).
11. Shang, X. F. et al. Biologically active isoquinoline alkaloids covering 2014-2018. *Med. Res. Rev.* **40**, 2212–2289 (2020).
12. Krey, A. K. & Hahn, F. E. Berberine: complex with DNA. *Science* **166**, 755–757 (1969).
13. Giri, P. & Kumar, G. S. Molecular aspects of small molecules-poly(A) interaction: an approach to RNA based drug design. *Curr. Med. Chem.* **16**, 965–987 (2009).
14. Chatterjee, S. & Suresh Kumar, G. Small molecule induced poly(A) single strand to self-structure conformational switching: evidence for the prominent role of H-bonding interactions. *Mol. Biosyst.* **13**, 1000–1009 (2017).
15. Kawano, M., Takagi, R., Kaneko, A. & Matsushita, S. Berberine is a dopamine D1- and D2-like receptor antagonist and ameliorates experimentally induced colitis by suppressing innate and adaptive immune responses. *J. Neuroimmunol.* **289**, 43–55 (2015).
16. Niwa, M., Mibu, H., Nozaki, M., Tsurumi, K. & Fujimura, H. Dopaminergic unique affinity of tetrahydroberberine and l-tetrahydroberberine-d-camphor sulfonate. *Pharmacology* **43**, 329–336 (1991).
17. Xu, P. et al. Structures of the human dopamine D3 receptor-G(i) complexes. *Mol. Cell* **81**, 1147–1159.e1144 (2021).
18. Crist, A. M. et al. Transcriptomic analysis to identify genes associated with selective hippocampal vulnerability in Alzheimer's disease. *Nat. Commun.* **12**, 2311 (2021).
19. Zhu, H. et al. The clinical characteristics and molecular mechanism of pituitary adenoma associated with meningioma. *J. Transl. Med.* **17**, 354 (2019).
20. Yildirim, M., Cengil, E., Eroglu, Y. & Cinar, A. Detection and classification of glioma, meningioma, pituitary tumor, and normal in brain magnetic resonance imaging using deep learning-based hybrid model. *Iran J. Comput. Sci.* **6**, 455–464 (2023).
21. Torabi, S. F. et al. RNA stabilization by a poly(A) tail 3'-end binding pocket and other modes of poly(A)-RNA interaction. *Science* **371**, eabe6523 (2021).
22. Li, J. et al. 3'-Poly(A) tail enhances siRNA activity against exogenous reporter genes in MCF-7 cells. *J. RNAi Gene Silencing* **2**, 195–204 (2006).
23. Mitton-Fry, R. M., DeGregorio, S. J., Wang, J., Steitz, T. A. & Steitz, J. A. Poly(A) tail recognition by a viral RNA element through assembly of a triple helix. *Science* **330**, 1244–1247 (2010).
24. van Rooy, I., Mastrobattista, E., Storm, G., Hennink, W. E. & Schiffelers, R. M. Comparison of five different targeting ligands to enhance accumulation of liposomes into the brain. *J. Control Release* **150**, 30–36 (2011).
25. Oller-Salvia, B. et al. MiniAp-4: a venom-inspired peptidomimetic for brain delivery. *Angew. Chem. Int. Ed. Engl.* **55**, 572–575 (2016).
26. Huile, G. et al. A cascade targeting strategy for brain neuroglial cells employing nanoparticles modified with angiopep-2 peptide and EGFP-EGF1 protein. *Biomaterials* **32**, 8669–8675 (2011).
27. Dos Santos Rodrigues, B., Arora, S., Kanekiyo, T. & Singh, J. Efficient neuronal targeting and transfection using RVG and transferrin-conjugated liposomes. *Brain Res.* **1734**, 146738 (2020).
28. Shen, J. et al. Poly(ethylene glycol)-block-poly(D,L-lactide acid) micelles anchored with angiopep-2 for brain-targeting delivery. *J. Drug Target.* **19**, 197–203 (2011).
29. Wang, L. & Ma, Q. Clinical benefits and pharmacology of scutellarin: a comprehensive review. *Pharm. Ther.* **190**, 105–127 (2018).
30. Bakun, P. et al. Tea-break with epigallocatechin gallate derivatives—powerful polyphenols of great potential for medicine. *Eur. J. Med. Chem.* **261**, 115820 (2023).
31. Habteyes, T. G. et al. Hierarchical self-assembly of carbon dots into high-aspect-ratio nanowires. *Nano Lett.* **23**, 9474–9481 (2023).

32. Gaillard, P. J. et al. Pharmacokinetics, brain delivery, and efficacy in brain tumor-bearing mice of glutathione pegylated liposomal doxorubicin (2B3-101). *PLoS ONE* **9**, e82331 (2014).

33. Ohno, M. et al. BACE1 gene deletion prevents neuron loss and memory deficits in 5XFAD APP/PS1 transgenic mice. *Neurobiol. Dis.* **26**, 134–145 (2007).

34. Gao, D. & Liu, Y. Berberine regulates endocrine function in mice with polycystic ovary syndrome through PI3K/Akt/GSK-3β insulin signaling pathway. *Trop. J. Pharm. Res.* **21**, 9 (2022).

35. Bajad, N. G. et al. Combined structure and ligand-based design of dual BACE-1/GSK-3β inhibitors for Alzheimer's disease. *Chem. Pap.* **76**, 7507–7524 (2022).

36. Au, L. et al. Cytokine release syndrome in a patient with colorectal cancer after vaccination with BNT162b2. *Nat. Med.* **27**, 1362–1366 (2021).

37. Yuan, Z. Y. et al. TATA boxes in gene transcription and poly (A) tails in mRNA stability: new perspective on the effects of berberine. *Sci. Rep.* **5**, 18326 (2015).

38. Yuan, Z. et al. Berberine inhibits mRNA degradation by promoting the interaction between the poly A tail and its binding protein PABP. *J. Chin. Pharm. Sci.* **26**, 53–62 (2017).

39. Hou, X., Zaks, T., Langer, R. & Dong, Y. Lipid nanoparticles for mRNA delivery. *Nat. Rev. Mater.* **6**, 1078–1094 (2021).

40. Debnath, D., Kumar, G. S. & Maiti, M. Circular dichroism studies of the structure of DNA complex with berberine. *J. Biomol. Struct. Dyn.* **9**, 61–79 (1991).

41. Saran, A., Srivastava, S., Coutinho, E. & Maiti, M. 1H NMR investigation of the interaction of berberine and sanguinarine with DNA. *Indian J. Biochem. Biophys.* **32**, 74–77 (1995).

42. Nandi, R., Debnath, D. & Maiti, M. Interactions of berberine with poly(A) and tRNA. *Biochim. Biophys. Acta* **1049**, 339–342 (1990).

43. Yadav, R. C. et al. Berberine, a strong polyriboadenylic acid binding plant alkaloid: spectroscopic, viscometric, and thermodynamic study. *Bioorg. Med. Chem.* **13**, 165–174 (2005).

44. Han, X. et al. Ligand-tethered lipid nanoparticles for targeted RNA delivery to treat liver fibrosis. *Nat. Commun.* **14**, 75 (2023).

45. Pattipeiluhu, R. et al. Anionic lipid nanoparticles preferentially deliver mRNA to the hepatic reticuloendothelial system. *Adv. Mater.* **34**, e2201095 (2022).

46. Kim, M. et al. Engineered ionizable lipid nanoparticles for targeted delivery of RNA therapeutics into different types of cells in the liver. *Sci. Adv.* **7**, eabf4298 (2021).

47. Böttger, R. et al. Lipid-based nanoparticle technologies for liver targeting. *Adv. Drug Deliv. Rev.* **154-155**, 79–101 (2020).

48. Sinegra, A. J., Evangelopoulos, M., Park, J., Huang, Z. & Mirkin, C. A. Lipid nanoparticle spherical nucleic acids for intracellular DNA and RNA delivery. *Nano Lett.* **21**, 6584–6591 (2021).

49. Lokugamage, M. P. et al. Optimization of lipid nanoparticles for the delivery of nebulized therapeutic mRNA to the lungs. *Nat. Biomed. Eng.* **5**, 1059–1068 (2021).

50. Radmand, A. et al. The transcriptional response to lung-targeting lipid nanoparticles in vivo. *Nano Lett.* **23**, 993–1002 (2023).

51. Okuyama, T. et al. Iduronate-2-sulfatase with anti-human transferrin receptor antibody for neuropathic mucopolysaccharidosis II: a phase 1/2 trial. *Mol. Ther.* **27**, 456–464 (2019).

52. Beola, L., Iturrioz-Rodríguez, N., Pucci, C., Bertorelli, R. & Ciofani, G. Drug-loaded lipid magnetic nanoparticles for combined local hyperthermia and chemotherapy against glioblastoma multiforme. *ACS Nano* **17**, 18441–18455 (2023).

53. Villa-Cedillo, S. A. et al. CDNF overexpression prevents motor-cognitive dysfunction by intrastriatal CPP-based delivery system in a Parkinson's disease animal model. *Neuropeptides* **102**, 102385 (2023).

54. Zhou, X. G. et al. Targeting microglial autophagic degradation of the NLRP3 inflammasome for identification of thonningianin A in Alzheimer's disease. *Inflamm. Regen.* **42**, 25 (2022).

55. Wei, W. et al. ICAM-5/Telencephalin is a functional entry receptor for enterovirus D68. *Cell Host Microbe* **20**, 631–641 (2016).

56. Davidson, R. C. et al. Gene disruption by biolistic transformation in serotype D strains of Cryptococcus neoformans. *Fungal Genet. Biol.* **29**, 38–48 (2000).

57. Wang, X. et al. Engineered liposomes targeting the gut-CNS Axis for comprehensive therapy of spinal cord injury. *J. Control Release* **331**, 390–403 (2021).

58. Chien, E. Y. et al. Structure of the human dopamine D3 receptor in complex with a D2/D3 selective antagonist. *Science* **330**, 1091–1095 (2010).

59. Link, T. M., Valentin-Hansen, P. & Brennan, R. G. Structure of Escherichia coli Hfq bound to polyriboadenylate RNA. *Proc. Natl Acad. Sci. USA* **106**, 19292–19297 (2009).

60. Delano, W. L. PyMOL: an open-source molecular graphics tool. *CCP4 Newsl. Protein Crystallogr.* **1**, 82–92 (2002).

61. Ravindranath, P. A., Forli, S., Goodsell, D. S., Olson, A. J. & Sanner, M. F. AutoDockFR: advances in protein-ligand docking with explicitly specified binding site flexibility. *PLoS Comput. Biol.* **11**, e1004586 (2015).

62. Trott, O. & Olson, A. J. AutoDock Vina: improving the speed and accuracy of docking with a new scoring function, efficient optimization, and multithreading. *J. Comput Chem.* **31**, 455–461 (2010).

63. Liu, Y. L. et al. Effects of l-tetrahydropalmatine on locomotor sensitization to oxycodone in mice. *Acta Pharm. Sin.* **26**, 533–538 (2005).

64. Assmann, J. C. et al. Isolation and cultivation of primary brain endothelial cells from adult mice. *Bio Protoc.* **7**, e2294 (2017).

65. Zhang, Y., Huo, M., Zhou, J. & Xie, S. PKSolver: an add-in program for pharmacokinetic and pharmacodynamic data analysis in Microsoft Excel. *Comput. Methods Prog. Biomed.* **99**, 306–314 (2010).

66. Puzzo, D., Lee, L., Palmeri, A., Calabrese, G. & Arancio, O. Behavioral assays with mouse models of Alzheimer's disease: practical considerations and guidelines. *Biochem. Pharmacol.* **88**, 450–467 (2014).

67. Auer, H. et al. The effects of frozen tissue storage conditions on the integrity of RNA and protein. *Biotech. Histochem.* **89**, 518–528 (2014).

68. Valo, E. et al. Effect of serum sample storage temperature on metabolomic and proteomic biomarkers. *Sci. Rep.* **12**, 4571 (2022).

69. Wu, L. P. et al. Crossing the blood-brain-barrier with nanoligand drug carriers self-assembled from a phage display peptide. *Nat. Commun.* **10**, 4635 (2019).

70. Jing, D. et al. Tissue clearing of both hard and soft tissue organs with the PEGASOS method. *Cell Res.* **28**, 803–818 (2018).

Acknowledgements

Author contributions

C.L., Z.-H.J., X.B., Q.G., X.W., X.Q., and L.-F.Y. conceived and designed the study. L.Y., S.Z., and S.W. performed the experiments and analyzed the data. C.L., Z.-H.J., X.B., Q.G., X.W., X.Q., and L.-F.Y. wrote the manuscript. All authors reviewed and approved the final manuscript.

Competing interests

The authors declare no competing interests.

Additional information

Supplementary information The online version contains supplementary material available at https://doi.org/10.1038/s41467-025-57488-0.

Correspondence and requests for materials should be addressed to Zhi-Hong Jiang or Chong Li.

Peer review information *Nature Communications* thanks the anonymous reviewers for their contribution to the peer review of this work. A peer review file is available.

Reprints and permissions information is available at http://www.nature.com/reprints

Publisher's note Springer Nature remains neutral with regard to jurisdictional claims in published maps and institutional affiliations.